



Fatigue crack growth behavior of marine steel under variable amplitude loading-combining DIC technique and SEM observation

Changzi Wang^{a,b}, Shuqing Wang^{a,b}, Lingjun Xie^{a,b}, Yaping Liu^{a,b}, Junlin Deng^c, Wentao He^{a,b,*}

^a College of Engineering, Ocean University of China, Qingdao 266100, China

^b Shandong Provincial Key Laboratory of Ocean Engineering, Ocean University of China, Qingdao 266100, China

^c School of Mechanical and Marine Engineering, Beibu Gulf University, Qinzhou, Guangxi 535011, China



ARTICLE INFO

Keywords:
DIC technique
FCG behavior
Overload retardation
Strain evolution

ABSTRACT

This paper experimentally studies the fatigue crack growth (FCG) behavior of AH36 grade marine steel under variable amplitude loading. FCG testing is conducted using compact tension specimens. Digital image correlation technique (DIC) is employed to study the evolution of strain distribution and cyclic fatigue characteristics. Fractographic analysis is performed to explore the overload retardation mechanism. Results indicate that the FCG rate varies significantly under overload application, leading to the extension of fatigue life by 1.03, 1.18 and 2.42 times under the overload ratios (OLRs) of 1.5, 2.0 and 2.5. Reasonable evaluation of the fatigue performance depends on the loading history. Extension of the fatigue life for periodic overload (POL) cases is not a simple superposition of that under two single ones, the interaction effect between the adjacent tensile overloads cannot be neglected. Greater plastic dissipated energy corresponds to more severe plastic deformation at larger OLRs and crack lengths. The larger strain accumulation at the crack tip should account for the greater FCG resistance and more evident overload retardation effect. The fresh fracture surface is destroyed at a certain region after overload due to the premature contact of the crack flanks, confirming that overload induced crack closure exists.

1. Introduction

Fatigue issues are inevitable for marine structures under the coupled action of the wave, current, and wind, which have become increasingly prominent issues in recent years with the upsizing of marine structures and wide application of high-strength steel [1]. The initiation and propagation of fatigue cracks can not only lead to insufficient reserve buoyancy due to the destruction of water-tightness but also induce the reduction of ultimate load-bearing capacity due to the destruction of structural integrity [2]. Therefore, it is essential to evaluate the fatigue performance of the marine structures through a fracture mechanics-based method, which is inseparable from a good understanding of the fatigue crack growth (FCG) characteristic of marine steels, especially considering the actual stochastic sea states with variable loading amplitude.

The FCG behavior depends strongly on the loading history, which may vary significantly with the loading amplitude and sequence, etc. The introduction of a single tensile overload in the constant amplitude

loading can usually be regarded as one of the most simplified loadings with variable amplitude, which has been employed by many scholars to study the transient FCG behavior and overload mechanism of diverse materials [3–5]. Several compelling intrinsic mechanisms have been proposed to explain the overload retardation effect, including the plasticity-induced closure effect [6,7], compressive residual stress ahead of crack tip [8], crack tip blunting [9] and strain hardening [10,11].

Although the study of the FCG behavior under a single overload contributes significantly to the investigation of the intrinsic mechanisms of the fatigue damage under variable loading, it may be oversimplified to ignore the interaction effects between the adjacent overloads considering the complex actual operating conditions. Investigations have reported that interaction effects are closely related to the relative loading magnitude and the sustained cycles between applied overloads. However, the majority of them were proposed based on the study of structural steels [12,13], railway steels [14,15], steam turbine blade materials [16], and aircraft materials [17–19], etc. The conclusions may not apply to AH36 grade high-strength marine steels due to the different

* Corresponding author at: College of Engineering, Ocean University of China, Qingdao 266100, China.

E-mail address: hewentao@ouc.edu.cn (W. He).

fatigue characteristics.

Factually, the FCG behavior under the variable amplitude loading is rather complicated and usually cannot be reasonably explained by a single mechanism. In order to gain a deep understanding of the internal mechanisms, experimental studies are definitely considered to be the most effective and convincing approach. Accurate observation and dynamic monitoring of the mechanical behavior of crack tips have been an inevitable challenge during the experimental implementation. Along with the development of the experimental techniques, challenges are also encountered to the traditional optical measurement methods. Higher requirements are put forward to gain the intuitive and quantitative results [20–22]. As an improvement, X-ray diffraction technique was proposed to observe the mechanical behavior at the crack tip and to calculate the local strain distribution through the crystal deformation theory combined with the elastic mechanics [23–25]. However, there are obvious limitations that arise during the practical applications. Cumulative plastic deformation could not be obtained, and the calculation accuracy was prone to be affected by the microstructure morphology (especially the grain size). The microgrid method is an advanced measurement technique that provides a new approach for rapid, accurate and reliable measurement of the material surface deformation [26]. The deformation field was calculated by comparing the progressive deformation of the microstructure with microgrids that were printed on the surface of the material, without any special requirements on the testing equipment. Unfortunately, microgrids preparation required an accurate etching with special advanced equipment, which inevitably increased the experimental costs and severely limited the applications. In addition, the microgrid distortion under large deformations might affect the accuracy of the calculation or even lead to an eventual failure of the calculation. Compared with the above-mentioned approaches, the digital image correlation (DIC) technique has the unique advantages of convenient operation, non-contact full-field measurement, strong anti-interference ability, high measurement accuracy, and loose requirements of experimental conditions [27]. Increasing more attempts have been made to observe the micro-deformation and crack tip behaviors [28–30]. Therefore, the DIC technique is employed to further investigate the intrinsic mechanisms of the FCG behavior and the cyclic fatigue characteristics under variable amplitude loading.

In this study, the FCG behavior and cyclic fatigue characteristic of the AH36 grade marine steel are experimentally studied in combination with the DIC technique. First, experimental studies are conducted using compact tension (CT) specimens to obtain the fracture parameters and characterize the overload retardation and interaction effects. Subsequently, the evolutions of the plastic zone and the strain distribution at the crack tip are investigated through the DIC technique to explore the intrinsic mechanism of the overload retardation. Additionally, the strain response at the crack tip is investigated to better obtain the cyclic fatigue characteristics through the characterization of the plastic dissipation energy and the strain accumulation over a loading cycle. Furthermore, the relationship between the fracture morphology and FCG behavior is studied through the fractographic analysis, and the retardation mechanism of the FCG rate is explored through the scanning electron microscope (SEM) observations.

2. Experimental details

2.1. Testing setup

The experiments are conducted in the lab air at room temperature according to the ASTM E647 standard using a servo-hydraulic MTS testing system with a dynamic load capacity of 25.0 kN and a maximum loading frequency of 30.0 Hz. The testing system is under computer control and can record the loading history in real time through the built-in sensor. To observe the local FCG characteristic, a microscope with a maximum magnification 270 \times is employed together with a charge coupled device (CCD) camera which can continuously take digital

images at a rate of 10 images per second. Setup of the testing system is illustrated in Fig. 1.

2.2. Material and specimen

Experimental study is implemented to gain the FCG behavior of the AH36 grade high-strength steel, which is extensively applied in the ship and marine engineering field. The chemical compositions and basic mechanical properties provided by the manufacturer are listed in Tables 1 and 2, respectively.

The FCG testing is conducted using standard CT specimens which are cut from the same base material along the rolling direction, with the dimensions of 62.5 × 60.0 × 8.2 mm. A knife-edge (notch) is machined at the right side to facilitate the installation of the extensometer. For easier initiation of the fatigue cracks, a 1.0 mm seam is machined at the notch through the wire cut electrical discharge machining (WEDM) with 0.012 mm molybdenum wire. All the specimens are polished to a degree of Ra0.8 for easier identification of the fatigue cracks. A simple demonstration of the geometrical dimensions and the machining process is shown in Fig. 2.

2.3. Experimental procedures

2.3.1. Pre-cracking

Pre-cracking is essential prior to the FCG testing to eliminate the effects of residual stress induced by machining work and the influence of blunt tip caused by WEDM. In this study, a total crack length of 13.0 mm is pre-cracked, corresponding to the SIF range of 12.42 MPa•m^(1/2) according to the description of,

$$\Delta K = \frac{\Delta P}{B\sqrt{W}} \frac{(2 + \alpha)}{(1 - \alpha)^{3/2}} (0.886 + 4.64\alpha - 13.32\alpha^2 + 14.72\alpha^3 - 5.6\alpha^4) \quad (1)$$

where ΔP is the applied loading amplitude; B and W correspond to the thickness and height of the specimens; α relates to the ratio of the current crack length a to the height of the specimen W , expressing as a/W .

2.3.2. FCG testing

Three types of the FCG testing are designed for the experimental study, including the constant amplitude loading (CAL) conditions, single overload (SOL) conditions, and periodic overload (POL) conditions. FCG testing plan and the corresponding parameters definition are listed in Table 3.

2.3.3. DIC analysis

DIC technique can obtain the structural deformation and strain distribution by tracking the deformation of the speckle pattern. Unique advantages are possessed by the DIC technique, such as the non-contact full and local measurement with visual results, etc. In this study, XTDIC three-dimensional full-field strain measurement system is employed for DIC calculation.

2.3.3.1. Definition of the reference and target images. As illustrated in Fig. 3(a), the reference images are set as the initial digital image of the loading cycle to be studied, corresponding to the deformation status under the baseline loading level of $P_{min} = 0.5$ kN. Different plans are designed for the target images of the CAL, SOL and POL cases to investigate the crack opening and closure responses, overload retardation and interaction effect. When collecting the digital images, the loading frequency is reduced to 0.1 Hz to ensure that enough images can be captured within the loading cycle. Considering the fact that crack tips are so sharp that artificial speckles made by the spray paint may not be accurate enough to ensure the calculation accuracy, natural polished texture of the specimen is applied for DIC analysis.

As a reference, a graduated scale is glued on the specimen surface along the potential crack path to facilitate the identification of the

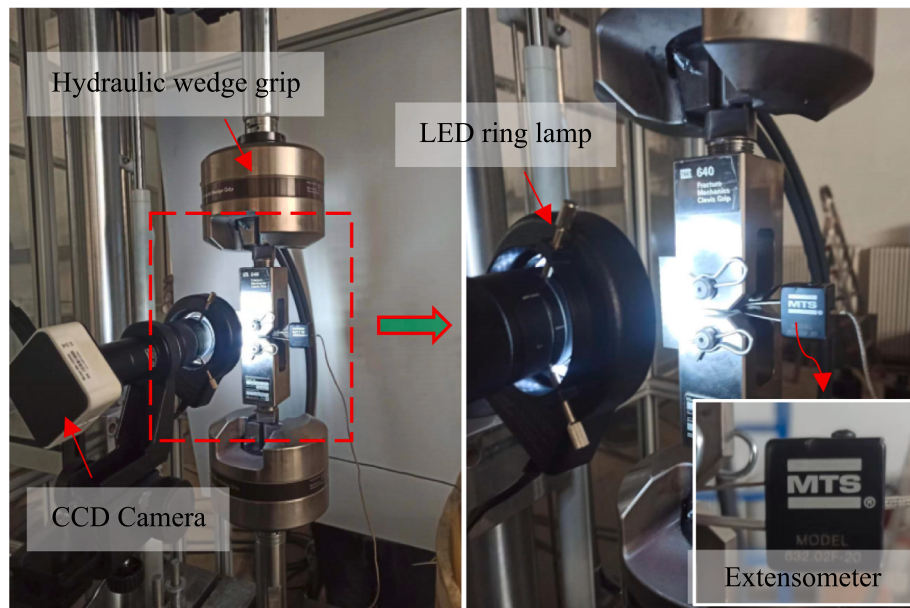


Fig. 1. Setup of the testing system.

Table 1
Chemical compositions of the AH36 steel (wt%).

C	Si	Mn	P	S	S_Al	V	Ti	Nb
0.16	0.28	1.35	0.021	0.005	0.027	0.00	0.016	0.03

Table 2
Material properties of the AH36 steel.

Material property	Value	Unit	Material property	Value	Unit
Density(ρ)	7847	kg/m ³	Yield strength (σ_y)	459	MPa
Modulus of elasticity (E)	206	GPa	Ultimate strength (σ_u)	558	MPa
Poisson's ratio (ν)	0.301	--	Elongation	29.5	%

camera's field of view, which is then removed to avoid shielding the region of interest before recording the images. Typical exhibition of the reference and target digital images are illustrated in Fig. 3(b) and (c). Both of them are captured through a 12-megapixel camera with a resolution of 4000×3000 , and each 100 pixels represent an actual dimension of about 0.1025 mm.

2.3.3.2. Crack tip locating method. Accurately locating the crack tips, which are usually very sharp and cannot be clearly identified even through the optical microscope, is a challenging issue. Therefore, a

method is proposed to accurately locate the crack tips based on the gradient of the displacement distribution, and the error is controlled within one pixel of the digital images.

As illustrated in Fig. 4(a) and (b), after preliminarily determining the approximate range of the crack tip, the displacement of the interested region is collected along the pixels in the X-direction. An increasingly obvious variation of the displacement appears as the pixel gradually approaches the crack tip. All the curves intersected at a pixel of $y = 116$ with a displacement value of 0.02138 mm. Subsequently, the displacement along the pixel of $y = 116$ is collected, as shown in Fig. 4(c) and (d). When the pixel reaches the crack region, the original distribution trend is interrupted with significant fluctuation, based on which the preliminary location of the crack tip can be determined. Then, according to the displacement value of 0.02138 mm, the pixel coordinate in the X-direction can be uniquely determined. Taking the exhibited case as an example, the coordinate of the crack tip can be determined to be (227, 116).

2.3.3.3. Virtual extensometer technology. To investigate the crack opening and closure responses, the crack opening displacement (COD) along the crack wake region is monitored using virtual extensometer technology. As shown in Fig. 5, several pairs of virtual extensometers with a distance of 0.18 mm are arranged, and the distance between the monitoring points is 0.2 mm.

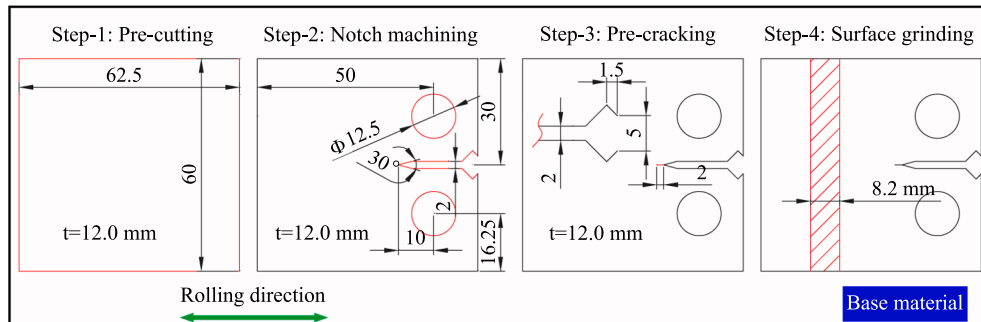


Fig. 2. Preparation process of the CT specimens.

Table 3
FCG testing plan.

Cases	Labels	P_{\min} (kN)	P_{\max} (kN)	R	P_{OL}	OLR	a_{OL} (mm)	ΔL (mm)
CAL	CAL-1	0.5	5	0.1	--	--	--	--
	SOL-1	0.5	5	0.1	7.5	1.5	19.0	--
SOL	SOL-2	0.5	5	0.1	10.0	2	19.0	--
	SOL-3	0.5	5	0.1	12.5	2.5	19.0	--
	POL	0.5	5	0.1	10.0	2.0	19.0	0.5
POL	POL-1	0.5	5	0.1	10.0	2.0	19.0	1
	POL-2	0.5	5	0.1	10.0	2.0	19.0	1.5
	POL-3	0.5	5	0.1	10.0	2.0	19.0	1.5

Parameters definition
Load ratio: $R = P_{\min}/P_{\max}$
Overload ratios: OLR = P_{OL}/P_{\max}

- a_{OL} : Crack length at overload; - ΔL : Crack increments;

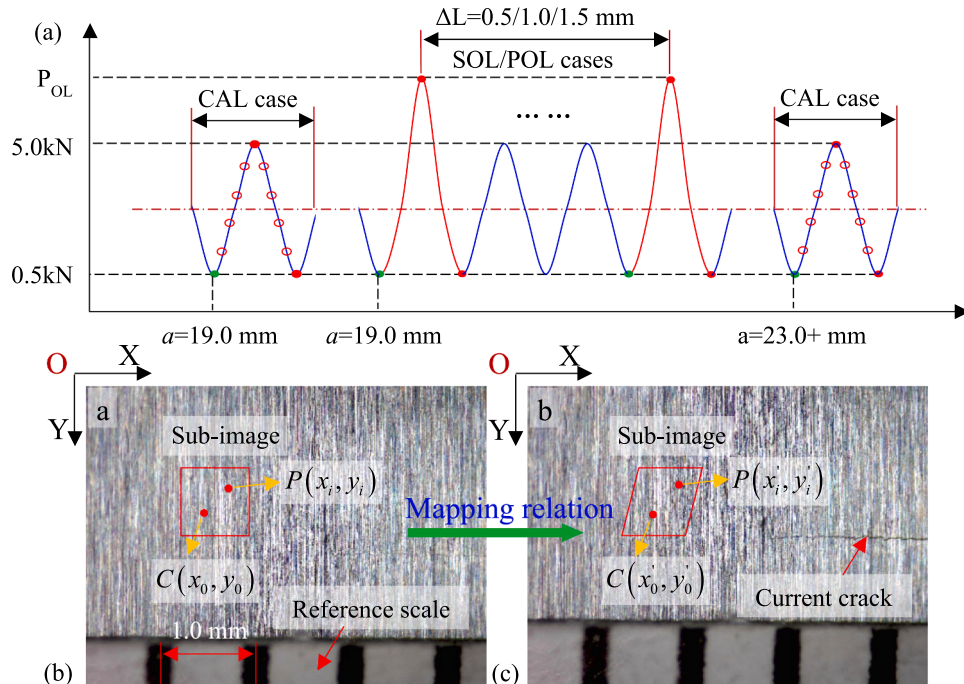


Fig. 3. Definition (a) and exhibition of the reference (b) and target (c) images.

2.3.4. SEM observation

To make a dynamic monitoring of the FCG process and make a macroscopic representation of the relationship between the fracture morphology and FCG behavior, fracture surface morphological analysis is implemented combining the SEM observation of the FCG path, crack tip morphology and crack section characteristics.

3. Results and discussion

The transient FCG behavior and the overload retardation effect of the FCG rate are investigated, considering the interaction effects between the adjacent overloads. Subsequently, the cyclic fatigue characteristic is investigated through the strain evolution at the crack tip under different overload ratios and at diverse crack lengths. Then, fracture surface morphological analysis is performed to relate the fracture morphology and FCG behavior and explore the retardation mechanism.

3.1. FCG behavior

3.1.1. FCG behavior under CAL case

Fig. 6 exhibits the FCG behavior and fatigue life of the CAL-1 case. As shown in Fig. 6(a), in addition to the crack initiation and the unstable growth stages, linear relationship is well maintained between the FCG rate (da/dN) and the SIF range (ΔK) in log-log scale. Based on the experimental results, Paris parameters C and m are determined to 3.1821×10^{-9} and 3.1395 respectively by the least squares linear fitting method. The crack growth in Fig. 6(b) shows an accelerated process, and the crack size grows exponentially with the loading cycle. The crack grows from 13.0 mm to 30.0 mm in 606,774 cycles and when the crack size reaches about 30.0 mm, the crack starts to propagate rapidly.

3.1.2. FCG behavior under SOL cases

Fig. 7 provides a comparison of the experimental results under diverse OLR cases, and that of the CAL-1 case is also included as a reference to investigate the induced retardation effect of the FCG rate and its influence on the fatigue life.

As shown in Fig. 7(a), similar to the description in ref. [31], several

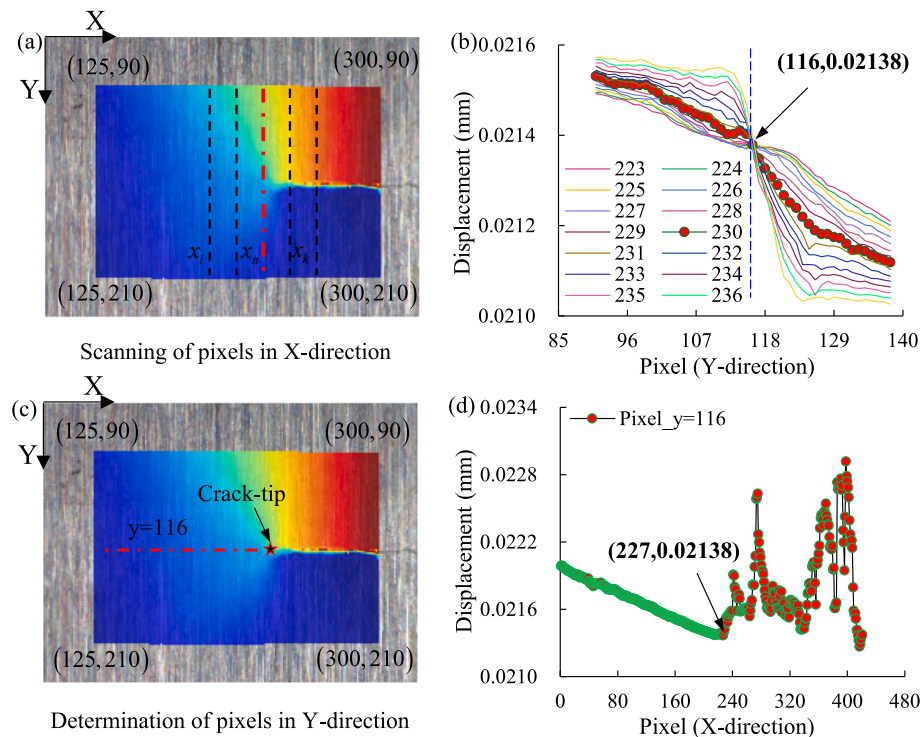


Fig. 4. Locating of the crack tip, (a)-(b) displacement collection along the pixels in X-direction; (c)-(d) displacement collection along the pixels in Y-direction.

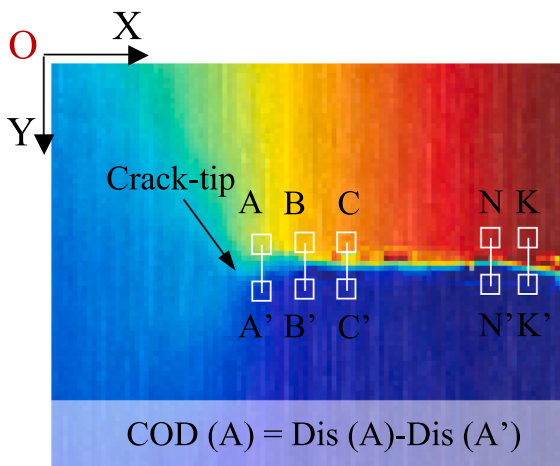


Fig. 5. Arrangement of the monitoring points.

stages of the FCG behavior can be identified including: (I) stable stage before overload; (II) instantaneous acceleration stage; (III) delayed retardation stage; (IV) retardation stage; (V) stable stage after overload. The FCG rate first experiences a stable linear growth stage before being interrupted by the overload application. Then, an instantaneous acceleration can be clearly identified right after the overload application, followed by an immediate reduction to the minimum value. When the FCG rate gradually recovers to the baseline level, the fatigue cracks keep growing stably again. FCG rates fit well with each other at the early stage before the overload application, indicating good consistency between different cases. With the increase of the OLR, the instantaneous acceleration of FCG rate becomes more evident, followed by an immediate larger reduction to the minimum value and longer recovery period to the baseline level. Regarding the stable stage after overload, good consistency is also obtained.

The transient acceleration of the FCG rate can be primarily attributed to the weakened crack closure and even the possible regional tearing after the overload application. The significant reduction of the FCG rate at the delayed retardation stage and the longer recovery period at the retardation stage can be primarily ascribed to the coupling effect of the strain redistribution and the crack tip behavior after tensile overload.

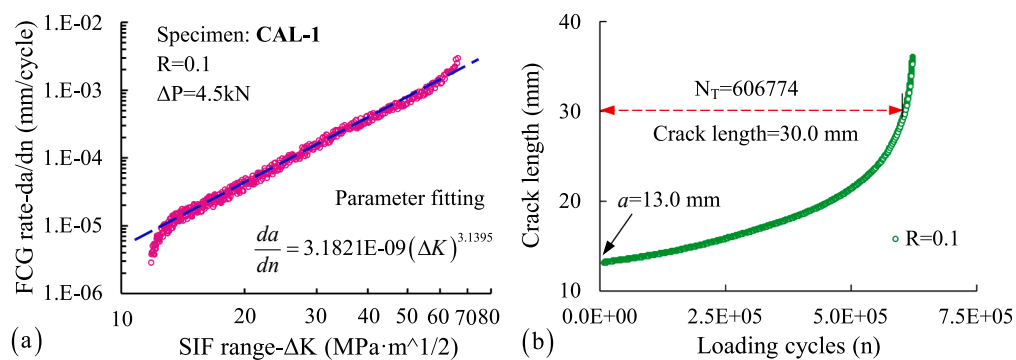


Fig. 6. FCG behavior (a) and fatigue life (b) of the CAL-1 case.

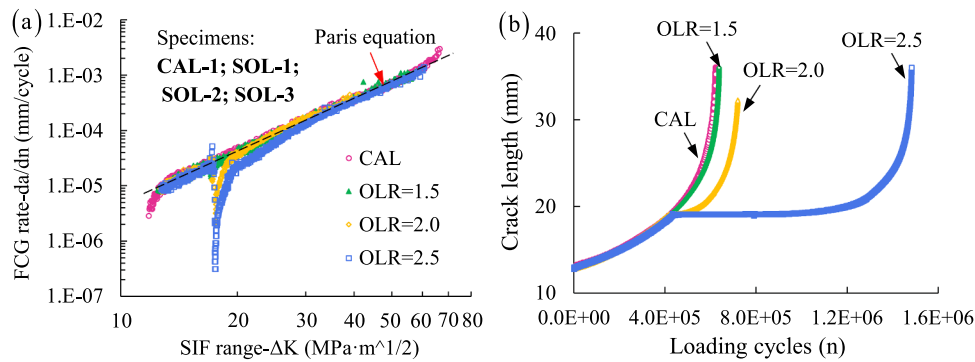


Fig. 7. Comparison of the FCG behavior (a) and fatigue life (b) of SOL cases.

Tensile overload may lead to the crack tip blunting, bifurcation and the appearance of secondary cracks, which may decrease the strain concentration and enlarge the crack length. Besides, a certain number of cycles are required to reinitiate and propagate the crack away from this blunted crack tip [32]. Additionally, the residual compressive strain after unloading may reduce the effective tensile stress and induce shielding effect of the FCG rate [4]. Moreover, the residual deformation at the crack wake region may lead to earlier closure of the crack and reduce the effective SIF value at the crack tip. The stable growth after overload corresponds to a stage without evident influence of the overload affected zone.

As illustrated in Fig. 7(b), good consistency of the fatigue life is achieved at the early stage of the FCG between the CAL-1 and SOL cases. Difference starts to appear right after the overload application due to the interruption of the original FCG trend. With the increase of the OLR, the final fatigue life increases, corresponding to the increasingly significant retardation effect. Primary results of the SOL cases are summarized in Table 4.

3.1.3. FCG behavior under POL cases

The application of a single tensile overload may be oversimplified for the engineering practice, since an accurate evaluation of the fatigue life is difficult to be obtained neglecting the interaction between the adjacent overloads. In this section, three POL cases are employed to investigate the interaction effect and mechanism of the FCG behavior, as shown in Fig. 8.

As can be seen in Fig. 8(a), at the steady stable growth stages before the first and after the second overload application, good consistency is obtained compared with those of the CAL-1 and SOL-2 cases. The instantaneous acceleration, delayed retardation, and the available retardation stages are in good agreement with each other between the SOL-2 and POL cases. However, when the second overload is applied, the original recovery process after the application of the first overload is

interrupted and the secondary instantaneous acceleration stage is activated, followed by the secondary delayed retardation and retardation stages. As the overload interval increases, the stages after the second overload are correspondingly prolonged.

Fig. 8(b) represents the fatigue life of the POL cases, and those of the CAL-1 and SOL-2 cases are also included to investigate the overload interaction effects. Two delays of the fatigue life can be clearly identified, leading to an extension of the final value compared with that of the SOL-2 case and of course the CAL-1 case.

Primary results of the POL cases are summarized in Table 5. Although the retardation effect of the FCG rate is further intensified due to the second overload application, the extension of fatigue life cannot be identified as a simple superposition of two single overloads. Interaction effects between the tensile overloads cannot be neglected when characterizing the FCG behavior and evaluating the fatigue life.

3.2. Strain evolution

For metallic materials with elastic–plastic constitutive behavior, the material near the crack tip yields rapidly under fatigue loading, forming a plastic zone. It is essential to study the evolution of the strain distribution for further investigation of the FCG behavior.

3.2.1. Strain evolution within a loading cycle

Fig. 9(a) and (b) provide a dynamic evolution of the strain distribution during the loading process that was calculated using DIC technique. As the fatigue loading increases sinusoidally from 0.5 to 5.0 kN, the plastic zone at the crack tip undergoes a process of emergence, intensification and aggravation until reaching a peak value. As the distance from the crack tip increases, the strain decreases rapidly from the maximum value to a low level near zero, presenting a more pronounced gradient under larger fatigue loading level. Additionally, the plastic strain region also enlarges, which is well-correlated with the increasing

Table 4
Primary results of the SOL cases.

Specimen labels	P _{min} (kN)	P _{max} (kN)	Overload application			Fatigue life (N _T)	Retardation description	
			OLR	a _{OL} (mm)	Cycle (N _{OL})			
SOL-1	0.5	5.0	1.5	19.0	416,000	625,200	18,426	1.03
SOL-2	0.5	5.0	2.0	19.0	414,000	713,161	106,387	1.18
SOL-3	0.5	5.0	2.5	19.0	433,607	1,470,698	863,924	2.42

Symbol clarification:	-N _{OL} : Fatigue life at the overload application;
	-N _{DCA} : Fatigue life extension compared with the CAL case;
	-N _T : Fatigue life from 13.0 to 30.0 mm in crack size;

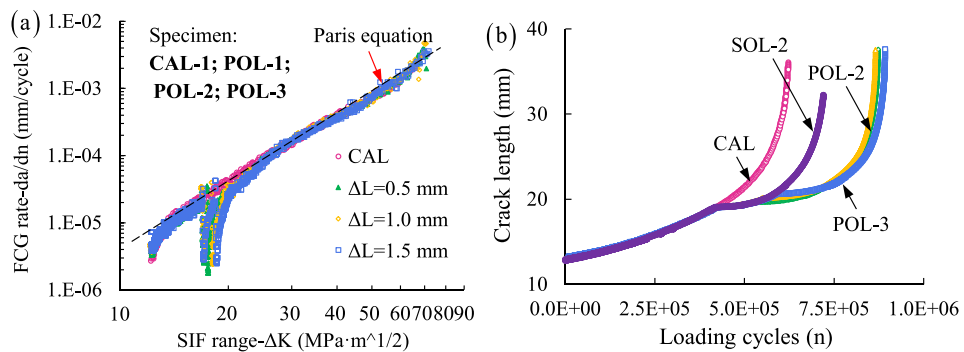


Fig. 8. Comparison of the FCG behavior (a) and fatigue life (b) of POL cases.

Table 5

Primary results of the POL cases.

Labels	P_{OL} (kN)	1st Overload		2nd Overload		Fatigue life (N_T)	Retardation description			
		a_{OL1} (mm)	N_{1st}	a_{OL2} (mm)	N_{2nd}		N_{SOL}	Prolonged	N_{DCA}	Prolonged
POL-1	10.0	19.0	426,985	19.5	524,985	859,429	146,268	1.21	252,655	1.42
POL-2	10.0	19.0	424,359	20.0	560,359	852,242	139,081	1.20	245,468	1.40
POL-3	10.0	19.0	421,627	20.5	593,627	878,264	165,103	1.23	271,490	1.44

Symbol clarification:

- a_{OL1} and N_{1st} : Crack size and the fatigue life at the first overload
- a_{OL2} and N_{2nd} : Crack size and the fatigue life at the second overload
- N_{SOL} : Fatigue life extension compared with the SOL case;

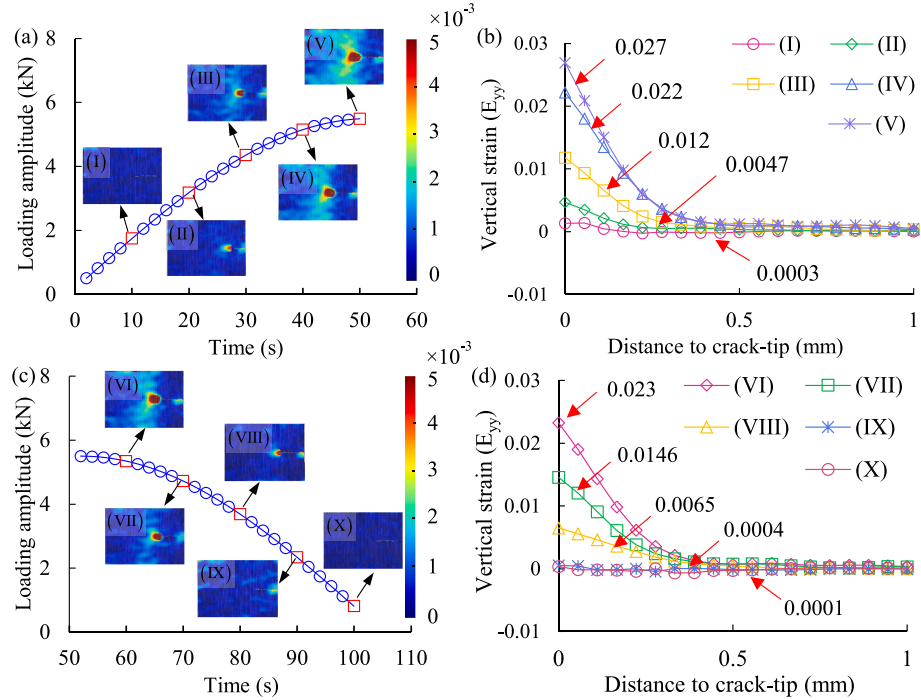


Fig. 9. Full-field strain distribution and strain variation ahead the crack tip during the loading process (a)-(b) and unloading process (c)-(d).

strain concentration at the crack tip.

As for the unloading process in Fig. 9(c) and (d), an evident opposite trend of the strain variation can be observed compared with that of the loading process. With the descending of the fatigue loading, strain localization at the crack tip gradually disappears, and strain gradient ahead of the crack tip is gradually weakened. When the fatigue loading is reduced to the baseline level, no evident plastic deformation can be identified.

3.2.2. Strain redistribution under a tensile overload

It is well known that, after an overload, the compressive residual stress field in the plastic zone of crack tip prevents the crack from propagating forward and produces the so-called 'shielding effect', which is usually recognized as a main factor controlling the crack propagation behavior [29]. Therefore, to gain more insight into the overload retardation mechanism, the longitudinal strain distribution under diverse OLR conditions is calculated using the DIC technique, as illustrated in

Fig. 10.

Fig. 10(a)–(c) display the strain distribution in the region of interest under the application of overload. For the OLR = 1.5 case, a tensile strain concentrates near the crack tip, which is mainly concentrated in a small region near the crack tip and distributed along the direction of about $\pm 45^\circ$ relative to the potential FCG path. Regarding the OLR = 2.0 case, the strain concentration zone is enlarged, presenting a kidney-shaped distribution. When the OLR is increased to 2.5, the strain concentration at the crack tip is further aggravated, and the kidney-shaped strain distribution extends to the entire width of the specimen.

Fig. 10(d)–(f) exhibit the residual strain distribution after complete unloading. Compressive residual strain appears at the crack tip and becomes increasingly evident with the increase of the OLR. For the OLR = 1.5 case, the strain is irregularly distributed at a low level, and no distinct strain concentration can be identified at the crack tip. Regarding the OLR = 2.0 case, an evident residual strain concentration appears at a small range near the crack tip and the irregularly distributed strain is intensified. When the OLR increases to 2.5, the residual strain concentration zone at the crack tip is further enlarged, accompanied by an extension of the high-level strain distribution.

Fig. 11 shows the strain distribution ahead of the crack tip. Obvious gradient of the strain can be observed, which becomes more evident under larger OLR, even after complete unloading. As the OLR increases from 1.5 to 2.0 and 2.5, the peak strain values under the overload application increase from 4.59% to 5.75% and 7.08%, while those after complete unloading increase from 0.05% to 0.20% and 0.39%, respectively.

3.2.3. Strain variation with FCG process

Fig. 12 illustrates the strain distribution at several crack sizes which is calculated through the DIC technique to further investigate the strain evolution during the FCG process. With the increase of the crack size, the strain concentration intensifies with a larger zone at the crack tip, forming an incompletely symmetric kidney-shaped strain distribution. The larger strain concentration region corresponds to the more evident plastic deformation at the crack tip, and the asymmetric distribution can mainly be attributed to the possible crack deflection under overload application [33].

3.3. Cyclic fatigue characteristic

Fatigue cracks are not initiated from the virgin material but from the previously damaged areas where fatigue damage occurs and accumulates inside a material. The FCG can be identified as a process with

dynamic variation of the material state, induced by the moving plastic zones at the crack tips where the fatigue damage is the severest [34], especially for the metallic materials with elastic-plastic constitutive behavior. Since the strain loops can provide a good indication of the cyclic fatigue characteristic, they are employed for characterizing the damage evolution of materials. The overload retardation mechanism and the FCG process are studied through the characterization of the plastic dissipated energy and damage accumulation within a loading cycle.

3.3.1. Strain response under overload application

Fig. 13 shows the strain responses of three SOL cases. Two stages of the ascending and descending can be observed within the overload cycle. With the increase of the OLR, obvious differences can be observed in terms of the peak strain values, the strain hysteresis loop, and the residual strain magnitudes.

For the OLR = 1.5 case in **Fig. 13(a)**, both the ascending and descending stages vary nearly linearly along the same path with a strain hysteresis loop of about 0. When the overload ratio increases to 1.5, the maximum value reaches 4.59%.

Regarding the strain response of the OLR = 2.0 case in **Fig. 13(b)**, several stages are experienced within a loading cycle, including elastic loading, yielding in tension, elastic unloading, and yielding in compression. As the fatigue loading increases, the strain first undergoes a short linear ascending stage and then enters into a phase with obvious plastic deformation until reaching a maximum value of 5.75% at P_{\max} of 10.0 kN. Subsequently, the strain starts to decrease linearly, followed by a reverse yielding stage as the fatigue loading decreases. Additionally, a clear deviation appears between the ascending and descending segments of the strain path, forming a distinct strain loop. The apparent area covered by the strain loop illustrates that energy is dissipated through the plastic deformation, resulting in a reduction of the effective driving force of the FCG. Moreover, the strain loop is no longer a closed one, as it remains unclosed at the bottom on a certain distance (0.038). This phenomenon indicates that strain accumulation appears within the overload cycle and regional tearing may also occur under the tensile overload with OLR = 2.0.

Referring to the OLR = 2.5 case in **Fig. 13(c)**, the strain hysteresis loop is further enlarged, accompanied with an increase of the maximum strain value (7.08%) and the gap (0.056) between the start and end points. These phenomena illustrate that the strain concentration is further intensified. Greater energy is dissipated through the plastic dissipation and larger accumulated strain is induced within a loading cycle. Both of them should account for the greater reduction of the

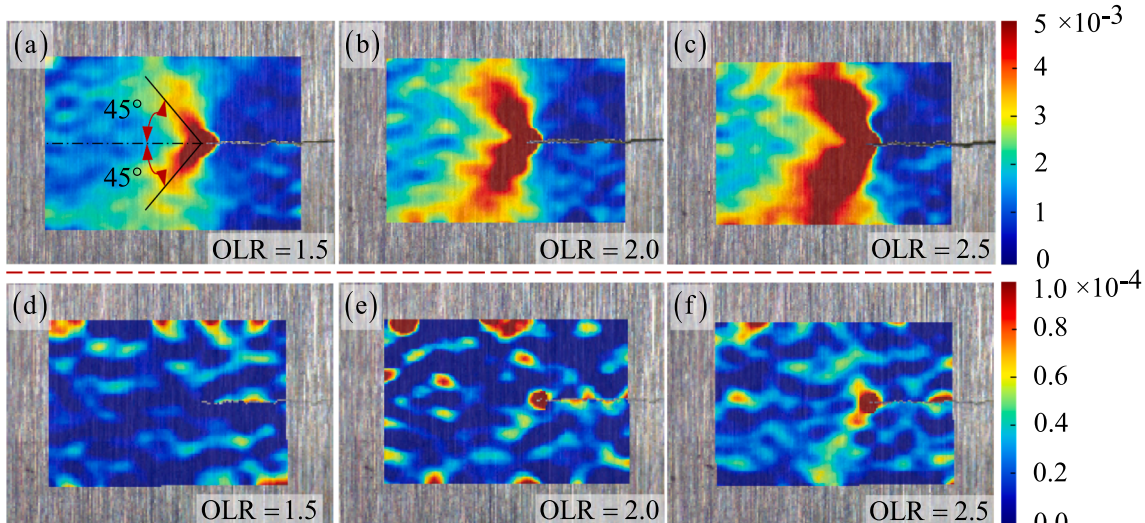


Fig. 10. Full-field strain distribution under the overload application (a)–(c) and after complete unloading (d)–(f).

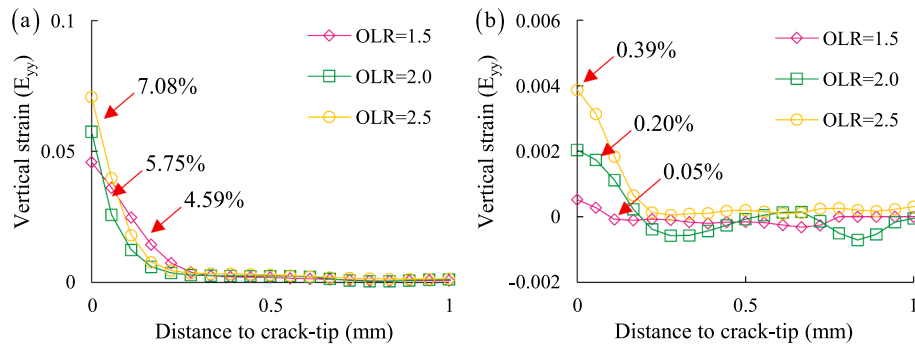


Fig. 11. Strain distribution ahead of the crack tip under the overload application (a) and after complete unloading (b).

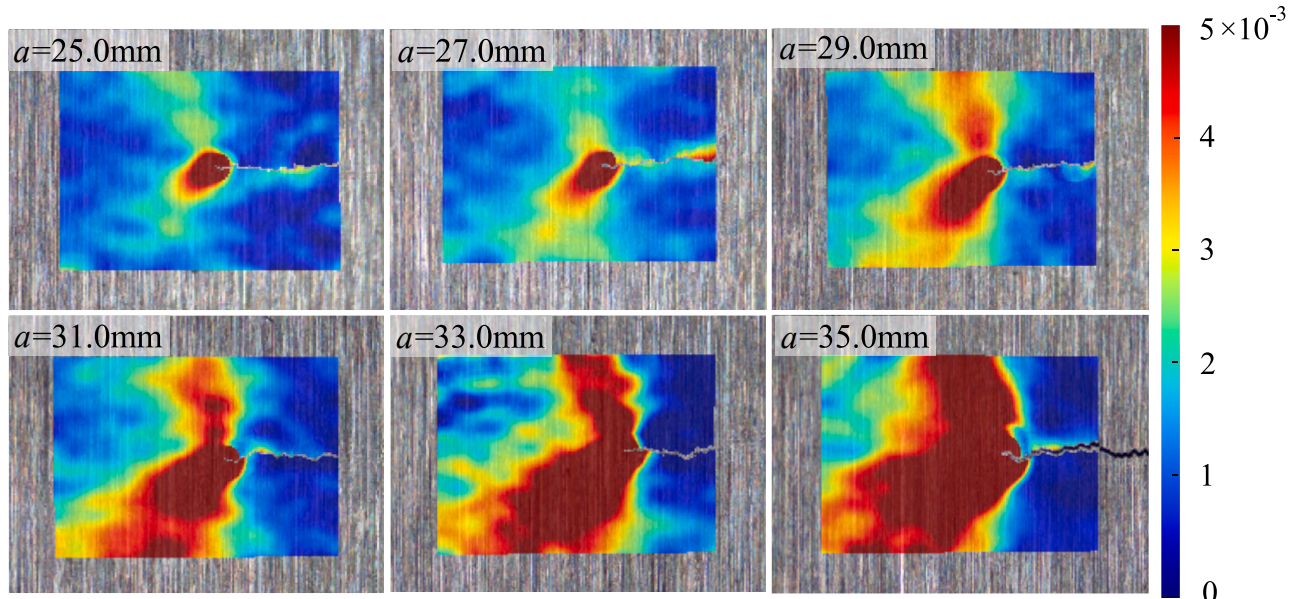


Fig. 12. Strain evolution with FCG process.

minimum value of the FCG rate and the longer recovery period of the retardation stage.

3.3.2. Strain response ahead of the crack tip

To obtain the dynamic strain evolution during the FCG process, the strain response ahead of the crack tip is studied in this section, as shown in Fig. 14. Fig. 14(a) shows the definition of 'A', 'B', 'C', and 'D' points that are collected at an increasing distance ahead the crack tip along the potential FCG path, and the corresponding strain responses are illustrated in Fig. 14(b).

As the distance from the crack tip increases, the maximum strain value reduces significantly, with a gradual decrease in amplitude. This phenomenon can primarily be attributed to the gradient of the strain distribution ahead of the crack tip, which gradually diminishes as the distance increases from the crack tip. Additionally, the strain hysteresis loop decreases from the point 'A' to 'D', and almost completely disappears from the point 'C'. The shrinking hysteresis illustrates that the energy dissipated through the plastic deformation is gradually reduced. The specimen is dominated by the linear deformation at the point 'C' and the position further away from the crack tip. Moreover, the gap at the bottom of the strain loop gradually decreases from the point 'A' to point 'D', as can be observed from the sub-figure of detail-'A'. This phenomenon indicates that the strain accumulation within a loading cycle gradually decreases from the point 'A' to point 'D', and no fatigue damage appears any more under the linear deformation at the locations

far away from the crack tip.

3.3.3. Strain response at diverse crack lengths

Fig. 15 shows the strain response at diverse crack lengths, which is employed to better understand the dynamic strain evolution during the FCG process. Due to the limited field of view of the camera, each strain loop is calculated taking the digital image at the starting moment of its respective cycle as a separate reference.

As the crack grows, the maximum strain value increases and the strain hysteresis loops are gradually enlarged; however, all the strain loops remain closed without discernible gaps at the bottom. The increased peak strain values can be primarily attributed to the enlarged arm from the loading axis to the crack tip and the reduction of the structural stiffness. The enlarged area covered by the strain hysteresis loops indicate that the plastic dissipation energy within a loading cycle increases gradually and more material at the crack tip undergoes plastic deformation. The closed strain loops illustrate that the residual strain is not apparent within a constant cyclic loading.

Comparing the strain loop at a crack length of 33.0 mm with those under tensile overload applications, all of them own large peak strain values and evident plastic dissipation energy. However, the FCG rate experiences a significant retardation under the application of tensile overload, while the crack continues to grow rapidly at a crack length of 33.0 mm. Therefore, the residual strain after unloading should be responsible for the different FCG behaviors due to its influence on the

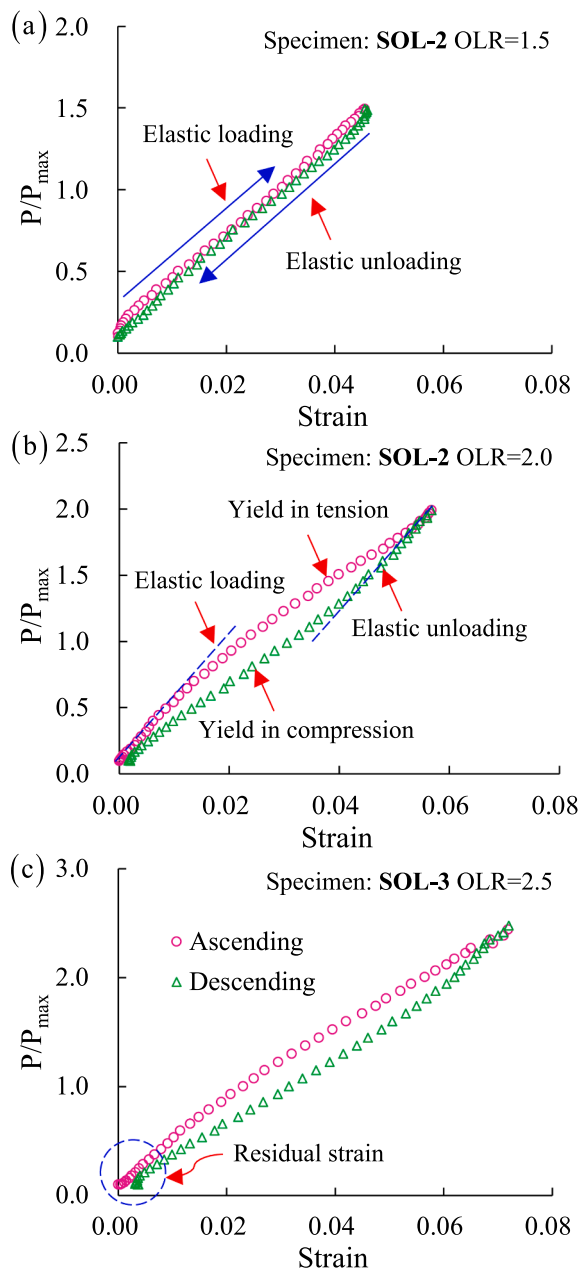


Fig. 13. Strain loops under the overload application of OLR = 1.5 (a), OLR = 2.0 (b) and OLR = 2.5 (c).

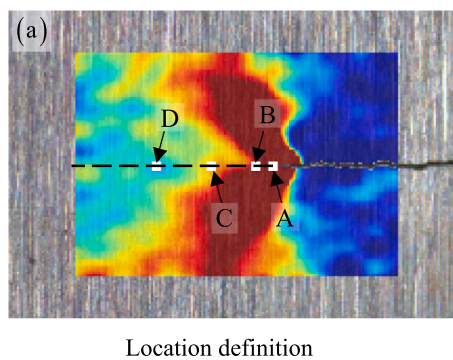


Fig. 14. Points definition (a) and strain loops (b) ahead of the crack tip.

variation of the plastic zone and the evolution of the residual plastic strain at the crack tip. The larger the residual plastic strain (or strain accumulation) appears at crack tip, the greater the resistance of the FCG and the stronger the overload retardation effect are.

3.4. Crack opening and closure responses

Fig. 16(a) shows the variation of the COD in the wake region at about 0.18 mm from the crack tip for SOL cases. When the fatigue loading decreases to the minimum value of 0.5 kN, residual COD appears, and its value increases with the increase of OLR.

Fig. 16(b) exhibits the crack opening profile of different OLR cases at the P_{OL} moment. As the OLR increases, the COD value is greater at a certain crack length due to the larger loading amplitude. Two segments can be identified for the entire crack profile: the rapid growth stage 'A' near the crack tip and the quasi-linear growth stage 'B' away from the crack tip. The evident gradient of the COD at the stage 'A' indicates that crack blunting appears at the crack tip due to the variation of the plastic zone. As for quasi-linear growth at the stage 'B', it corresponds to a region with weakened influence of the overload affected zone, where the material is primarily under elastic deformation.

3.5. Fracture surface morphological analysis

Since the DIC technique is implemented by tracking the deformation of the speckle pattern, the actual crack tip behavior may not be obtained due to the failure of fully capturing the fracture surface morphology. Further investigation is essential through the morphological analysis.

Fig. 17 shows the fracture surface observed by SEM near the overload position. As shown in **Fig. 17(a)** and (b), the crack front which separates the fracture surface with distinct behavior before and after the overload

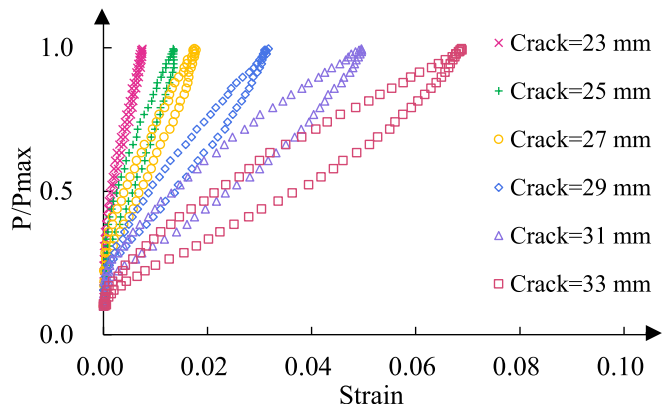
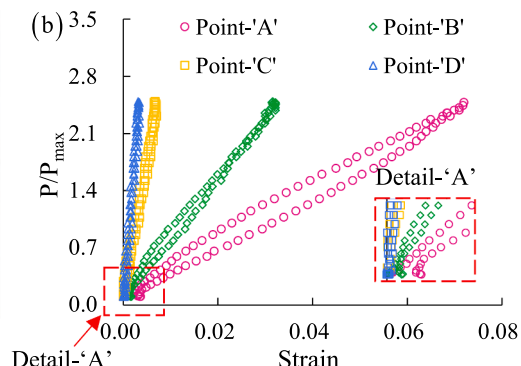


Fig. 15. Strain response at the crack tip at diverse crack lengths.



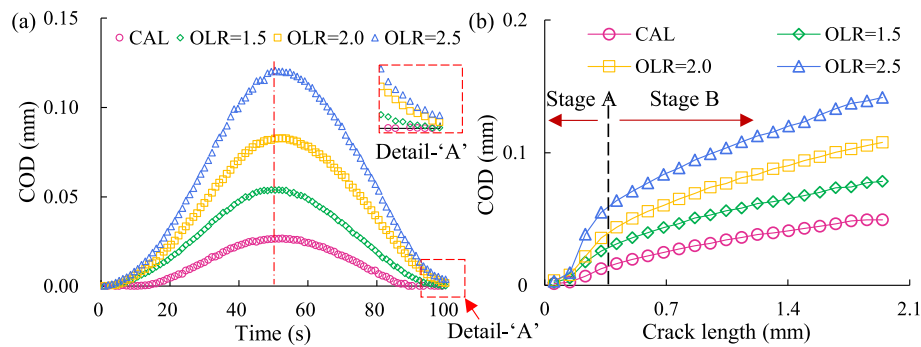


Fig. 16. Exhibition of the residual COD (a) and crack opening profile (b).

application can be clearly identified. Fine elongated lines can be observed before the overload line, while a relative smooth and flat region appears after the overload line without evident observation of the fatigue striations. This phenomenon confirms that the overload induced crack closure exists which may lead to the premature contact of the crack flanks and destroy the fresh fracture surface. Secondary cracks, voids and tearing ridges/edges can be identified along the overload line in the further magnified images in Fig. 17(c)-(d). The appearance of the regional tearing ridges should account for the transient acceleration of the FCG rate due to the instantaneous overload that exceeded the fracture resistance of the AH36 grade steel. Secondary cracks reduce the effective driving force. The ductile tear may lead to the blunting of the crack tip and further the decohesion of grain boundaries [33]. The void indicates that larger plastic zone is induced, and more energy is consumed when reshaping to its original form during the recovering process [35]. The coupling effect of them should be responsible for the reduced FCG rate after overload application.

Fig. 18(a)–(c) exhibits the fracture surfaces at different crack lengths along the FCG direction. Comparing with the overload location, the fatigue striations and the secondary cracks can be more clearly identified at the points 'A', 'B' and 'C', accompanied by distinct secondary cracks. Additionally, it can be observed that local ductile tearing exists during the FCG process, even at small crack sizes before the overload

application. As for the final tearing region, the whole fracture surface presents dimples, as illustrated in Fig. 18(d).

4. Conclusions

In this study, experiments are conducted to investigate the fatigue crack growth (FCG) behavior of the AH36 marine steel under variable amplitude loading. The overload retardation mechanism is investigated through the characterization of the cyclic fatigue characteristics and the fracture surface morphological analysis, combining DIC technique and SEM observations. Based on the above-mentioned study, several conclusions are drawn:

- (1) For the CT specimen under OLRs of 1.5, 2.0 and 2.5, fatigue lives are prolonged by 1.03, 1.18 and 2.42 times comparing with that of the CAL case under the load ratio of $R = 0.1$. Reasonable fatigue evaluation depends closely on the loading history.
- (2) Extension of the fatigue life is not a simple superposition of that under two single overloads, accurate evaluation of the fatigue cannot be obtained neglecting the interaction effects between the adjacent tensile overloads.
- (3) A method is developed to determine the accurate location of the crack tip and obtain the crack size from the displacement

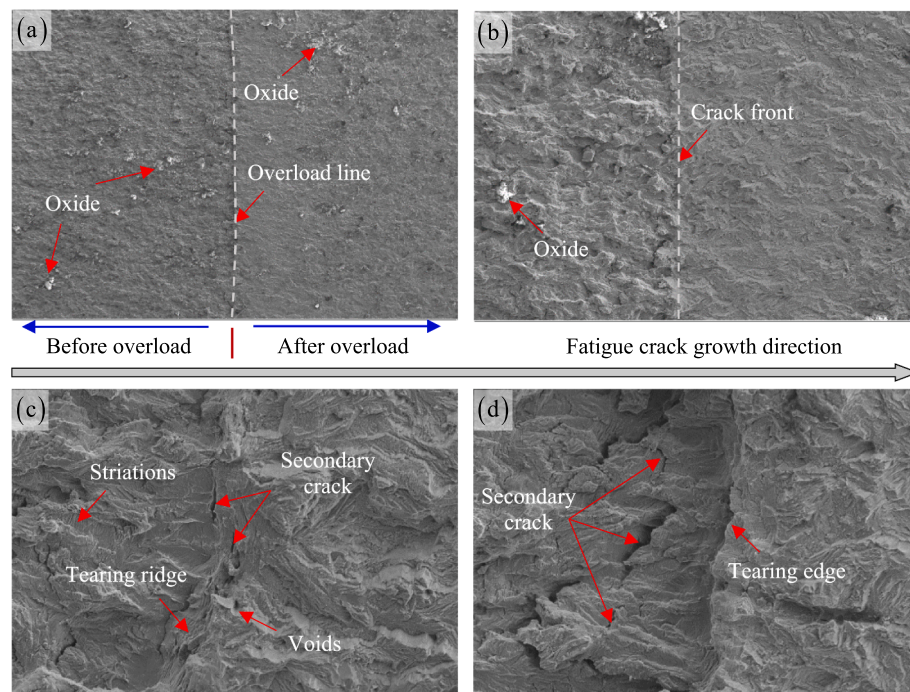


Fig. 17. Observations of the fracture surfaces at overload location with 50× (a), 200× (b), 1000× (c) and 2000× (d).

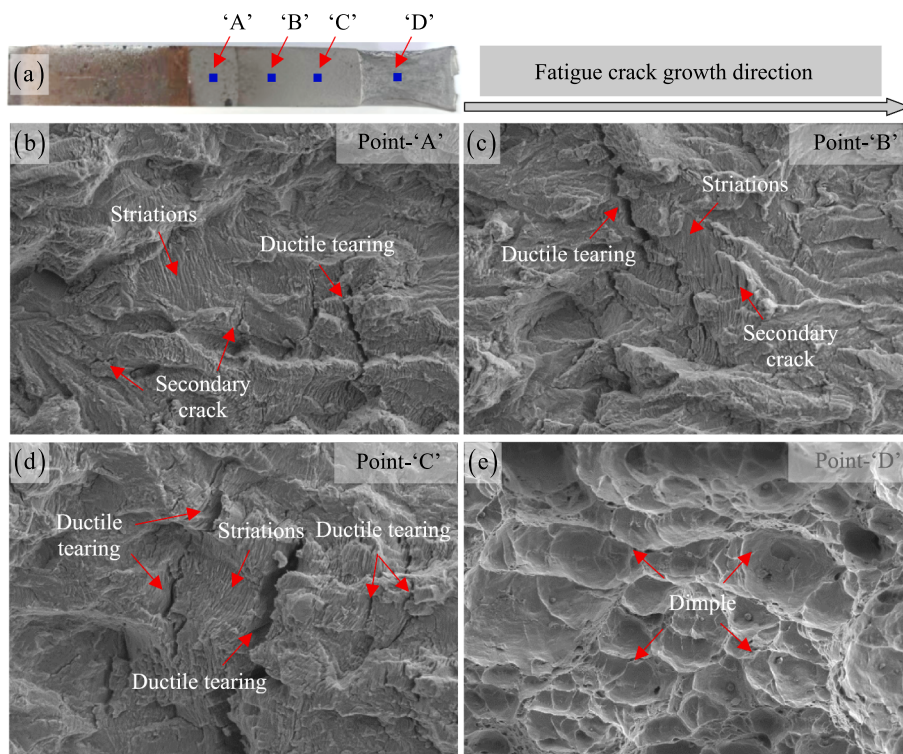


Fig. 18. Point definition (a) and fracture surfaces observation at different crack lengths (b)–(e).

distribution of the specimen. The larger strain accumulation at the crack tip should account for the greater FCG resistance and more evident overload retardation effect.

- (4) The fresh fracture surface is destroyed at a certain region after overload application due to the premature contact of the crack flanks. The overload retardation is related to the crack closure effect for the AH36 grade marine steel.

Declaration of Competing Interest

The authors declare that they have no known competing financial interests or personal relationships that could have appeared to influence the work reported in this paper.

Data availability

Data will be made available on request.

Acknowledgements

The present work is supported by the National Natural Science Foundation of China (Grant Nos. 52071308, 51879248, 51879249, 52161042 and 51609089), the China Postdoctoral Science Foundation (Grant No. 2016M592338), and the Guangxi Natural Science Foundation (Grant No. 2021GXNSFAA075003).

References

- [1] He W, Xie L, Wang S, Wang C, Hu Z, Liu J. Fatigue characterization analysis of a submerged fishing farm platform through spectral-based fracture mechanics. *Ocean Eng* 2022;264:112351.
- [2] Cui W, Huang X, Wang F. Towards a unified fatigue life prediction method for marine structures. Berlin Heidelberg: Springer; 2014.
- [3] Wu Y, Bao R. Fatigue crack tip strain evolution and crack growth prediction under single overload in laser melting deposited Ti-6.5 Al-3.5 Mo-1.5 Zr-0.3 Si titanium alloy. *Int J Fatigue* 2018;116:462–72.
- [4] Xie LQ, Zhang P, He XH, Zhou CY. Effect of single tensile overload on fatigue crack growth behavior of CP-Ti at negative load ratio. *Int J Fatigue* 2021;145:106129.
- [5] Li S, Zhang Y, Qi L, Kang Y. Effect of single tensile overload on fatigue crack growth behavior in DP780 dual phase steel. *Int J Fatigue* 2018;106:49–55.
- [6] Elber W. Fatigue crack closure under cyclic tension. *Eng Fract Mech* 1970;2(1):37–45.
- [7] Solanki K, Daniewicz SR, Newman Jr JC. Finite element analysis of plasticity-induced fatigue crack closure: an overview. *Eng Fract Mech* 2004;71(2):149–71.
- [8] Sunder A, Andronik A, Biakov A, Eremin A, Panin S, Savkin A. Combined action of crack closure and residual stress under periodic overloads: a fractographic analysis. *Int J Fatigue* 2016;82:667–75.
- [9] Rice JR. Mechanics of crack tip deformation and extension by fatigue 1967;415:247–309.
- [10] Pantelakis SG, Kermanidis TB, Pavlou DG. Fatigue crack growth retardation assessment of 2024-T3 and 6061-T6 aluminium specimens. *Theor Appl Fract Mech* 1995;22(1):35–42.
- [11] Pavlou DG. Prediction of fatigue crack growth under real stress histories. *Eng Struct* 2000;22(12):1707–13.
- [12] Liang H, Zhan R, Wang D, Deng C, Guo B, Xu X. Fatigue crack growth under overload/underload in different strength structural steels. *J Constr Steel Res* 2022;192:107213.
- [13] Skorupa M, Schijve J, Skorupa A, Machniewicz T. Fatigue crack growth in a structural steel under single and multiple periodic overload cycles. *Fatigue Fract Eng M* 1999;22(10):879–87.
- [14] Nejad RM. The effects of periodic overloads on fatigue crack growth in a pearlitic Grade 900A steel used in railway applications. *Eng Fail Anal* 2020;115:104687.
- [15] Nejad RM, Berto F. Fatigue crack growth of a railway wheel steel and fatigue life prediction under spectrum loading conditions. *Int J Fatigue* 2022;157:106722.
- [16] Cunningham BM, Evangelou A, You C, Morris A, Wise J, Reed PA, et al. Fatigue crack initiation and growth behavior in a notch with periodic overloads in the low-cycle fatigue regime of FV566 ex-service steam turbine blade material. *Fatigue Fract Eng M* 2022;45(2):546–64.
- [17] Fleck NA. Fatigue crack growth due to periodic underloads and overloads. *Acta Metall* 1985;33(7):1339–54.
- [18] Sarkheil S, Foumani MS. Numerical and experimental study on the optimization of overload parameters for the increase of fatigue life. *Aerospace Sci Technol* 2014;35:80–6.
- [19] Daneshpour S, Koçak M, Langlade S, Horstmann M. Effect of overload on fatigue crack retardation of aerospace Al-alloy laser welds using crack tip plasticity analysis. *Int J Fatigue* 2009;31(10):1603–12.
- [20] Christopher CJ, James MN, Patterson EA, Tee KF. A quantitative evaluation of fatigue crack shielding forces using photoelasticity. *Eng Fract Mech* 2008;75(14):4190–9.
- [21] Christopher CJ, James MN, Patterson EA, Tee KF. Towards a new model of crack tip stress fields. *Int J Fatigue* 2007;148(4):361–71.
- [22] James MN, Christopher CJ, Lu Y, Patterson EA. Local crack plasticity and its influences on the global elastic stress field. *Int J Fatigue* 2013;46:4–15.

- [23] Croft M, Shukla V, Jisrawi NM, Zhong Z, Sadangi RK, Holtz RL, et al. Mapping and load response of overload strain fields: synchrotron X-ray measurements. *Int J Fatigue* 2009;31:1669–77.
- [24] Lopez-Crespo P, Steuwer A, Buslaps T, Tai YH, Lopez-Moreno A, Yates JR, et al. Measuring overload effects during fatigue crack growth in bainitic steel by synchrotron X-ray diffraction. *Int J Fatigue* 2015;71:11–6.
- [25] Steuwer A, Rahman M, Shterenlikht A, Fitzpatrick ME, Edwards L, Withers PJ. The evolution of crack tip stresses during a fatigue overload event. *Acta Mater* 2010;58:4039–52.
- [26] Ghadbeigi H, Pinna C, Celotto S. Quantitative strain analysis of the large deformation at the scale of microstructure: comparison between digital image correlation and microgrid techniques. *Exp Mech* 2012;52(9):1483–92.
- [27] Wang C, Yao L, He W, Cui X, Wu J, Xie D. Effect of elliptical notches on mechanical response and progressive damage of FMs under tensile loading. *Thin Wall Struct* 2020;154:106866.
- [28] Salvati E, O'Connor S, Sui T, Nowell D, Korsunsky AM. A study of overload effect on fatigue crack propagation using EBSD, FIB-DIC and FEM methods. *Eng Fract Mech* 2016;167:210–23.
- [29] Chen R, Zhu ML, Xuan FZ, Wu SC, Fu YN. Near-tip strain evolution and crack closure of growing fatigue crack under a single tensile overload. *Int J Fatigue* 2020;134:105478.
- [30] Nowell D, Dragnevski KI, O'Connor SJ. Investigation of fatigue crack models by micro-scale measurement of crack tip deformation. *Int J Fatigue* 2018;115:20–6.
- [31] He W, Wang C, Deng J, Xie D, Zhang Z. Effect of single tensile overload on fatigue crack growth behavior based on plastically dissipated energy and critical distance theory. *Eng Fract Mech* 2020;223:106744.
- [32] Antunes FV, Castanheira FA, Branco R. A numerical analysis of the mechanisms behind plasticity induced crack closure: application to variable amplitude loadings. *Int J Fatigue* 2016;89:43–52.
- [33] Albedah A, Bouiadra BB, Mohammed SMAK, Benyahia F. Fractographic analysis of the overload effect on fatigue crack growth in 2024-T3 and 7075-T6 Al alloys. *Int J Min Met Mater* 2020;27(1):83–90.
- [34] Gonzales GLG, González JAO, de Castro JTP, de França Freire JL. Measuring elastoplastic strain loops in the near crack-tip region using a Stereo Microscope DIC system. *Int J Fatigue* 2020;133:105427.
- [35] Ren D, Xue Z, Jiang Y, Hu X, Zhang Y. Influence of single tensile overload on fatigue crack propagation behavior of the selective laser melting inconel 625 superalloy. *Eng Fract Mech* 2020;239:107305.